



# Deep and rapid observations of strong-lensing galaxy clusters within the sky localization of GW170814

G. P. Smith<sup>1</sup> <sup>1</sup>★ M. Bianconi,<sup>1</sup> M. Jauzac,<sup>2,3,4</sup> J. Richard,<sup>5</sup> A. Robertson<sup>1</sup> <sup>3</sup>, C. P. L. Berry<sup>1</sup> <sup>6</sup> R. Massey<sup>1</sup> <sup>2</sup> K. Sharon<sup>1</sup> <sup>7</sup> W. M. Farr<sup>8,9</sup> and J. Veitch<sup>10</sup>

<sup>1</sup>School of Physics and Astronomy, University of Birmingham, Birmingham B15 2TT, UK

<sup>2</sup>Centre for Extragalactic Astronomy, Department of Physics, Durham University, Durham DH1 3LE, UK

<sup>3</sup>Institute for Computational Cosmology, Durham University, South Road, Durham DH1 3LE, UK

<sup>4</sup>Astrophysics and Cosmology Research Unit, School of Mathematical Sciences, University of KwaZulu-Natal, Durban 4041, South Africa

<sup>5</sup>Univ Lyon, Univ Lyon1, Ens de Lyon, CNRS, Centre de Recherche Astrophysique de Lyon UMR5574, F-69230 Saint-Genis-Laval, France

<sup>6</sup>Center for Interdisciplinary Exploration & Research in Astrophysics (CIERA), Northwestern University, Evanston, IL 60208, USA

<sup>7</sup>Department of Astronomy, University of Michigan, 1085 S. University Avenue, Ann Arbor, MI 48109, USA

<sup>8</sup>Department of Physics and Astronomy, Stony Brook University, Stony Brook, NY 11794, USA

<sup>9</sup>Center for Computational Astrophysics, Flatiron Institute, 162 Fifth Avenue, New York, NY 10010, USA

<sup>10</sup>School of Physics and Astronomy, University of Glasgow, Glasgow G12 8QQ, UK

Accepted 2019 February 13. Received 2019 February 13; in original form 2018 May 18

## ABSTRACT

We present observations of two strong-lensing galaxy clusters located within the 90 per cent credible sky localization maps released following LIGO–Virgo’s discovery of the binary black hole (BH–BH) gravitational wave (GW) source GW170814. Our objectives were (1) to search for candidate electromagnetic (EM) counterparts to GW170814 under the hypothesis that it was strongly lensed, and thus more distant and less massive than inferred by LIGO–Virgo, and (2) to demonstrate the feasibility of rapid target of opportunity observations to search for faint lensed transient point sources in crowded cluster cores located within GW sky localizations. Commencing 20 h after discovery, and continuing over 12 nights, we observed Abell 3084 ( $z = 0.22$ ) and SMACS J0304.3 – 4401 ( $z = 0.46$ ) with GMOS on the Gemini-South telescope, and Abell 3084 with MUSE on ESO’s Very Large Telescope. We detect no candidate EM counterparts in these data. Calibration of our photometric analysis methods using simulations yields  $5\sigma$  detection limits for transients in difference images of the cores of these clusters of  $i = 25$ . This is the most sensitive photometric search to date for counterparts to GW sources, and rules out the possibility that GW170814 was lensed by these clusters with a kilonova-like EM counterpart. Based on the detector frame masses of the compact objects, and assuming that at least one neutron star (NS) is required in the merging system to produce a kilonova-like counterpart, implies that GW170814 was neither an NS–NS nor NS–BH merger at  $z > 8$  lensed by either of these clusters. Also, in the first ever emission line search for counterparts to GW sources, we detected no lines down to a  $5\sigma$  detection limit of  $5 \times 10^{-17}$  erg s $^{-1}$  cm $^{-2}$ .

**Key words:** gravitational lensing: strong – gravitational waves – gravitational waves: individual: GW170814 – galaxies: clusters: individual Abell 3084, SMACS J0304.3 – 4401.

## 1 INTRODUCTION

Observational astronomy gained a new tool with the first direct detection of gravitational waves (GWs; Abbott et al. 2016c). GWs have already provided new insights into the properties of compact binaries and the nature of gravity (e.g. Abbott et al. 2016d,f, 2017a, 2018a) that complement those accessible to EM observations. In

the case of GW170817 (Abbott et al. 2017c), the first GW signal from a binary neutron star (NS–NS) coalescence was followed by observations of a counterpart across the electromagnetic (EM) spectrum (Abbott et al. 2017e). These multimessenger observations permitted new tests of general relativity (Abbott et al. 2017f), measurement of the Hubble constant (Abbott et al. 2017d, 2018c), and yielded information on NS physics (e.g. Abbott et al. 2017g; Bauswein et al. 2017; Levan et al. 2017; Margalit & Metzger 2017).

Optical follow-up observations of stellar mass compact binary coalescence (CBC) sources of GWs are challenging because of

\* E-mail: [gps@star.sr.bham.ac.uk](mailto:gps@star.sr.bham.ac.uk)

the large sky localization uncertainties inherent in the LIGO–Virgo data analysis. With only two GW detectors, sky localizations can be  $\sim 100\text{--}1000 \text{ deg}^2$  (Singer et al. 2014; Berry et al. 2015); adding additional detectors to the network improves sky localization (Veitch et al. 2012; Abbott et al. 2016b; Pankow et al. 2018) and enhances 3D localization (Singer et al. 2016; Del Pozzo et al. 2018). Towards the end of LIGO–Virgo’s second observing run (O2) in 2017, when all three detectors were operational, the sky localizations from LIGO and Virgo for their triple-detector observations were  $\sim 20\text{--}90 \text{ deg}^2$  (Abbott et al. 2017b,c, 2018b). The largest cameras on 4-m and 8-m class optical telescopes have fields of view of up to a few square degrees. It is therefore time consuming to search thoroughly the error regions of even the best localized GW sources, especially in the case of binary black hole (BH–BH) mergers, for which any EM counterparts are expected to be faint or non-existent. Despite these challenges, early observations of BH–BH merger sky localization error regions have been invaluable testing grounds for optical follow-up (e.g. Abbott et al. 2016g; Cowperthwaite et al. 2016; Soares-Santos et al. 2016; Yoshida et al. 2017; Doctor et al. 2018; Utsumi et al. 2018). Strategies that aim to overcome the challenges include optimizing the tiling and scheduling of wide-field searches (Coughlin et al. 2018), and targeting the follow-up observations on stellar mass selected galaxies located within the 3D GW localizations (Nissanke, Kasliwal & Georgieva 2013; Fan, Messenger & Heng 2014; Hanna, Mandel & Vossen 2014; Gehrels et al. 2016). The latter approach was deployed to great success in the earliest identification of the optical counterpart to the NS–NS signal GW170817 (Coulter et al. 2017).

The luminosity distance to CBC sources is measured to 30–40 per cent precision from LIGO–Virgo data (Berry et al. 2015; Abbott et al. 2016e, 2018b). Gravitational lensing, and in particular strong lensing (i.e. multiple imaging), is a possible source of systematic bias in these inferred luminosity distances because the amplitude of the strain signal  $A$  depends on both lens magnification  $\mu$ , and luminosity distance  $D_L$ :  $A \propto |\mu|^{0.5} D_L^{-1}$  (hereafter we use  $\mu$  to denote  $|\mu|$ ). Therefore, lens magnification allows sources from greater distances to be observed, and also means that the luminosity distance to a lensed source inferred assuming  $\mu = 1$  is underestimated by a factor  $\mu^{0.5}$  (Wang, Stebbins & Turner 1996). The redshift distribution of the known galaxy and cluster strong lenses peaks close to  $z = 0.3$  (e.g. Smith et al. 2018b), which corresponds to a luminosity distance of  $D_L = 1.6 \text{ Gpc}$ . For a GW source that is initially interpreted as being located at  $D_L \lesssim 500 \text{ Mpc}$  to be reinterpreted as being strongly lensed implies that it must be magnified by a factor of  $\mu \gtrsim 10$ . The systematic bias in the inferred distance also means that the masses of the source, which are calculated using the inferred source redshift (Krolak & Schutz 1987), are overestimated by a factor  $(1 + z_{\mu=1})/(1 + z)$ , where  $z_{\mu=1}$  is the redshift inferred assuming  $\mu = 1$ , and  $z$  is the true redshift of the lensed source. Therefore, while lensing does complicate the measurement of distance, identification of a lensed source with LIGO–Virgo would provide a glimpse of the CBC population at  $z \gtrsim 1$ , well in advance of third-generation GW detectors.

A strongly lensed GW would travel to the Earth along multiple paths through the foreground mass concentration, and thus in principle could be detected on more than one occasion by LIGO–Virgo, as would any EM counterpart. These paths differ in length, leading to a time delay between detections of consecutive signals up to several years (Smith et al. 2018b). Multiple detections of a single GW source, will create unique scientific opportunities with important advantages over previous work and important new challenges to

overcome. The transient nature of GW events/detections mean that EM follow-up observations will not require expensive long-term monitoring programmes that are typical of time delay cosmography with lensed quasars. Moreover, the submillisecond precision to which the arrival time of GW signals is measured by LIGO–Virgo (Abbott et al. 2016a,d,e, 2017a) will lead to a measured precision on the time delay between the arrival of lensed GW signals that is  $\gtrsim 8$  orders of magnitude superior to that achievable with supernovae or quasars (e.g. Fohlmeister et al. 2007; Rodney et al. 2016). Therefore, in principle, strongly lensed GWs will yield unprecedented constraints on the distribution of dark and luminous matter in the gravitational lens, and a new and highly accurate measurement of the Hubble parameter (Liao et al. 2017). However, lens substructure and micro-lensing may reduce the precision of such measurements (Suyu et al. 2018 and references therein; Chen et al. 2018; Tie & Kochanek 2018), and therefore work to address such issues will be required. Comparing the time delay between EM and GW images will also enable the propagation speed of light and gravity to be compared (Collett & Bacon 2017; Fan et al. 2017). Multiple detections of the same GW source will also enable new constraints on GW polarizations because the number of detectors that observe the same GW signal would grow with the number of the detections of the strongly lensed event (cf. Chatzioannou, Yunes & Cornish 2012).

The probability that a GW source detected to date by LIGO–Virgo is strongly lensed is small because a tiny fraction of the sky is magnified sufficiently ( $\mu \gtrsim 10$ , as discussed above) to reinterpret the detected strain signal as originating from a source beyond the lens population. For example, Hilbert et al. (2008) estimate that the source plane optical depth to  $\mu > 10$  for sources at  $z \leq 2$  is  $\tau_s \gtrsim 10^{-5}$ . Therefore, whilst estimates for the rate of detection of lensed GW sources vary, there is a broad consensus that the expected rate during O1 and O2 is  $\ll 1 \text{ yr}^{-1}$ , and will rise to  $\gtrsim 1 \text{ yr}^{-1}$  when LIGO–Virgo reach design sensitivity in the early 2020s (Li et al. 2018; Ng et al. 2018; Smith et al. 2018b,a).

It will be difficult to identify that a GW source is strongly lensed from the LIGO–Virgo signal alone (Hannuksela et al. 2019). This is because the overestimated mass of the compact objects may not appear anomalous, and the GW sky localization uncertainties dwarf the solid angle subtended by the strong-lensing regions of galaxies, groups, and clusters by many orders of magnitude. Therefore, strong evidence beyond that available from the strain signal measured by LIGO–Virgo will be needed to outweigh the low prior expectation that a given GW signal was strongly lensed. Identification of an EM counterpart to a GW source adjacent to the critical curve of a strong lens, and detection of a subsequent image of the same source would provide such evidence, and thus establish that a GW had been strongly lensed. This would allow the correct source parameters to be inferred, and enable the science outlined above.

Current observations and theoretical predictions point to galaxy clusters dominating the optical depth to gravitationally magnifying point sources by  $\mu \geq 10$ . On the observational side, all strongly lensed images of quasars found by the Sloan Digital Sky Survey (SDSS) that are magnified by  $\mu > 10$  are lensed by galaxy clusters (Inada et al. 2003; Sharon et al. 2005, 2017; Oguri 2010, 2013). In contrast, individual galaxy lenses have thus far been shown to produce only low magnification strongly lensed quasar images, i.e.  $\mu < 10$  (Oguri et al. 2004, 2005, 2008; Inada et al. 2005, 2006, 2007, 2008, 2009, 2014; Kayo et al. 2007, 2010; Morokuma et al. 2007; Ofek et al. 2007; McGreer et al. 2010; Rusu et al. 2011, 2013; More et al. 2016; Agnello et al. 2018). This picture is supported by theoretical work, notably that of Hilbert et al. (2008), whose

optical depth to strong lensing is dominated by haloes of mass  $M_{200} > 10^{13} M_\odot$ , i.e. galaxy groups and clusters. However, the number of highly magnified quasars seen by SDSS is small, and Hilbert et al.'s predictions pre-date modern cosmological hydrodynamical simulations. Therefore, more theoretical and observational work is needed to clarify the relative contribution of galaxy- and cluster-scale haloes to high-magnification lensing of point sources such as CBCs. In Robertson et al. (in preparation), we will consider the optical depth to strong lensing as a function of halo mass based on cosmological hydrodynamical simulations, and in this article we concentrate on optical observations that explore the strong-lensing interpretation of BH–BH mergers detected by LIGO–Virgo.

We introduce a new observing strategy for identifying optical counterparts to GW sources – observations of strong-lensing galaxy cluster cores located within LIGO–Virgo GW sky localization maps. We describe our first implementation of this strategy via rapid target of opportunity (ToO) observations with the Gemini-South telescope<sup>1</sup> and ESO's Very Large Telescope<sup>2</sup> (VLT) in the nights immediately following the discovery of the BH–BH source GW170814 (Abbott et al. 2017b). Our observations targeted known strong-lensing galaxy clusters, selected from the list compiled by Smith et al. (2018b). The main goals of our observations were to test the feasibility of searching for optical transients in rapid follow-up observations with small field-of-view instruments (which are well matched to cluster cores, and not routinely used for discovery of transient objects) on 8-m class telescopes, and to search in earnest for candidate EM counterparts to putative strongly lensed GW sources. The large aperture of Gemini-South and VLT, and the absence of any requirement for us to explore the wider sky localization, enabled us to conduct deep observations that are sensitive to strongly lensed EM counterparts down to  $i = 25$  independent of the actual source redshift. Our strategy therefore benefits from greater sensitivity than conventional searches, at the expense of a much smaller survey volume.

We describe the details of our observing strategy, observations, and data reduction in Section 2, explain how we generate difference images, and search for candidate optical counterparts, and state our results in Section 3, discuss our results in Section 4, and summarize in Section 5. We assume a flat cosmology with  $H_0 = 67.9 \text{ km s}^{-1} \text{ Mpc}^{-1}$ ,  $\Omega_M = 0.3065$  (Ade et al. 2016). All celestial coordinates are stated at the J2000 epoch, and all magnitudes are stated in the AB system.

## 2 OBSERVATIONS

### 2.1 Observing strategy

We aim to conduct the most sensitive search to date for optical emission from CBC sources of GWs, under the hypothesis that the objects that we target have been strongly lensed by a massive foreground galaxy cluster. We therefore select known, spectroscopically confirmed strong-lensing clusters located close to the

<sup>1</sup>Based on observations obtained at the Gemini Observatory, which is operated by the Association of Universities for Research in Astronomy, Inc., under a cooperative agreement with the NSF on behalf of the Gemini partnership: the National Science Foundation (United States), the National Research Council (Canada), CONICYT (Chile), Ministerio de Ciencia, Tecnología e Innovación Productiva (Argentina), and Ministério da Ciência, Tecnologia e Inovação (Brazil).

<sup>2</sup>Based on observations made with ESO Telescopes at the La Silla Paranal Observatory under programme ID 299.A-5028.

peak probability of the sky localizations of LIGO Scientific-Virgo Collaboration (LVC) CBC alerts. The strong-lensing regions of these clusters span  $\sim 1\text{--}2 \text{ arcmin}^2$  on the sky, and are thus perfectly matched to instruments on ground-based 8-m class telescopes, including the GMOS instruments on the Gemini-North and South telescopes, and MUSE on VLT.

The most common GW sources are the coalescence of BH–BHs. Optical emission from BH–BHs is expected to be faint or non-existent (Abbott et al. 2016b, and references therein). Searches for optical emission from BH–BH mergers have typically reached sensitivity limits in the observer-frame  $V/R/I$ -bands of  $m \lesssim 22$  with telescopes up to 4 m in diameter and  $m \simeq 22\text{--}24$  with the Subaru 8-m telescope (e.g. Cowperthwaite et al. 2016; Soares-Santos et al. 2016; Arcavi et al. 2017; Yoshida et al. 2017; Doctor et al. 2018; Utsumi et al. 2018). In general, these observations reached a sensitivity compatible with detecting a kilonova-like counterpart to the respective BH–BH mergers and, as discussed in Section 1, their main aim was to implement and test a new type of observing campaign. We therefore adopted a nominal goal of reaching a spectral flux density limit with GMOS and MUSE corresponding to  $i \simeq 25$ , in order to push the sensitivity of EM follow-up observations into a new regime, independent of any lens magnification. In particular, we note that Doctor et al. (2018) observed the sky localization of GW170814 to a depth of  $i \simeq 23$  with the Dark Energy Camera. Moreover, after taking account of lens magnification of (say)  $\mu \simeq 100$ , the depth to which we observe corresponds to a search for optical emission from BH–BHs down to  $i \simeq 25 + 2.5\log(\mu) = 30$ .

Our observations are guided by the best localizations provided by the LVC at the time. Localizations are refined as improved analyses become available (Abbott et al. 2016b), but since we expect a kilonova-like optical counterpart to fade rapidly, it is not possible to delay follow-up observations until final localizations are communicated. We identify the clusters for potential observations by comparing the celestial coordinates of 130 strong-lensing clusters selected by Smith et al. (2018b) with the LVC sky localization. We use the 2D sky localization to prioritize the most promising observing targets. Typically, we pick the strong-lensing cluster closest to the peak of the probability distribution as the most promising to observe.

Our ToO observing programmes at the Gemini Observatory and European Southern Observatory (hereafter ESO) commenced in early 2017 August under programme IDs GN-2017A-DD-9, GS-2017A-DD-6, and 299.A-5028, respectively. These programmes allowed for up to 7 epochs of imaging observations with the GMOS instruments on the Gemini-North and Gemini-South telescopes, and up to 3 epochs of integral field spectroscopy with MUSE on VLT. The observations commence as soon as possible after receipt of the LVC alert via a rapid ToO, and were planned to extend over a period of one week following the alert via regular ToO observations.

### 2.2 Identification of strong-lensing clusters in the GW170814 sky localization

GW170814 was detected by LIGO and Virgo on 2017 August 14 at 10:30:43 UTC, and first announced via GCN circular on 2017 August 14 at 12:28:42 UTC (LIGO Scientific Collaboration and Virgo Collaboration 2017a) with an initial false alarm rate of  $\sim 1$  in 80 000 yr. The 90 per cent credible region in the initial BAYESTAR (Singer & Price 2016) sky localization spanned  $97 \text{ deg}^2$ , centred at celestial coordinates of  $(\alpha, \delta) = (02:44:00, -45:29:00)$ . We identified one strong-lensing cluster, Abell 3084 (Table 1), within

**Table 1.** Abell 3084 and SMACS J0304.3 – 4401.

	Abell 3084	SMACS J0304
Cluster redshift	0.22	0.46
Right ascension	03:04:07	03:04:21
Declination	-36:56:36	-44:01:48
$L_X[0.1\text{--}2.4\text{keV}] (10^{44}\text{erg s}^{-1})$	$4.0 \pm 0.6^a$	$7.1 \pm 0.2^b$
Redshift of multiple-image system	0.764 <sup>c</sup>	1.963 <sup>d</sup>

<sup>a</sup> Böhringer et al. (2004)<sup>b</sup> Repp & Ebeling (2018)<sup>c</sup> May (2013)<sup>d</sup> Christensen et al. (2012)

the 90 per cent credible region of the BAYESTAR map. Abell 3084 lies on the contour encircling a region within which the sky localization probability is  $p = 0.8$ , and which subtends  $57.5 \text{ deg}^2$  (Fig. 1).

As the LVC analyses were refined, the localization region evolved (Fig. 1). On 2017 August 16 at 07:02:19 UTC, the sky localization was updated based on the results of LALINFERENCe (Veitch et al. 2015), with a revised peak close to celestial coordinates of  $(\alpha, \delta) = (03:06:00, -44:36:00)$  and a 90 per cent credible region spanning  $190 \text{ deg}^2$  (LIGO Scientific Collaboration and Virgo Collaboration 2017b). We identified two strong-lensing clusters within the 90 per cent credible region of the LALINFERENCe map. Abell 3084 lay on the contour encircling  $p = 0.873$  per cent of the localization probability density, corresponding to a region subtending  $154.4 \text{ deg}^2$  – i.e. this cluster is further from the peak of the probability distribution following the update. SMACS J0304.3 – 4401 (Table 1) was closer to the peak of the probability distribution, on the contour that encloses  $p = 0.05$  of the sky localization probability and subtends  $2.1 \text{ deg}^2$ .

When GW170814 was first announced outside the LVC and EM follow-up partners in 2017 October (Abbott et al. 2017b), the best sky localization peaked close to  $(\alpha, \delta) = (03:10:00, -44:51:00)$ , with a 90 per cent credible region spanning  $60 \text{ deg}^2$ , and a luminosity distance of  $D_L = 540_{-210}^{+130} \text{ Mpc}$ . With this, Abell 3084 lay on the  $p = 0.994$  contour that subtends  $170.4 \text{ deg}^2$ , and SMACS J0304.3 – 4401 lay on the  $p = 0.57$  contour that subtends

$16.1 \text{ deg}^2$ . Subsequently, the LIGO–Virgo data were recalibrated and cleaned for the O2 Catalogue results (Abbott et al. 2018b). Analysis of these improved data gave a localization peaking close to  $(\alpha, \delta) = (03:09:00, -44:36:00)$  with a 90 per cent credible region spanning  $90 \text{ deg}^2$ , and a luminosity distance of  $D_L = 580_{-210}^{+160} \text{ Mpc}$ . With this, Abell 3084 lay on the  $p = 0.96$  contour that subtends  $170.2 \text{ deg}^2$ , and SMACS J0304.3 – 4401 lay on the  $p = 0.30$  contour that subtends  $7.7 \text{ deg}^2$ .

### 2.3 Abell 3084 and SMACS J0304.3 – 4401

Abell 3084 and SMACS J0304.3 – 4401 are X-ray luminous galaxy clusters at intermediate redshift (Table 1). Virial mass estimates of both clusters are not published to date, however, their X-ray luminosities are consistent with them both having a mass of  $M_{200} \simeq 10^{15} M_\odot$ . Both are spectroscopically confirmed strong lenses, each with one multiple-image system confirmed to date. Detailed models of the mass distribution in the cluster cores (May 2013; Christensen et al. 2012) are vital to interpreting the sensitivity of our observations and any flux that we detect from a candidate EM counterpart. The models are most accurate for sources at redshifts similar to the known multiple-image system redshifts; we therefore concentrate on these redshifts when considering the efficiency of our search for candidate EM counterparts in Section 3. *Hubble Space Telescope* (*HST*) snapshot observations with the Advanced Camera for Surveys (ACS) are available for both clusters, through the F606W filter (PID:10881 and 12166). We use these data to calibrate our GMOS and MUSE observations (Sections 2.5 and 2.6) and in our difference image analysis (Section 3.1).

### 2.4 Gemini and VLT observations

We observed Abell 3084 with GMOS on Gemini-S on five occasions, commencing 20 h after the first LVC alert pertaining to GW170814, on 2017 August 15 UTC. This was the first Chilean night following the detection of GW170814. The GMOS observations of Abell 3084 continued after the revised sky map became available, in order to obtain a comprehensive data set on one cluster. We also observed SMACS J0304.3 – 4401 with GMOS on Gemini-S on two

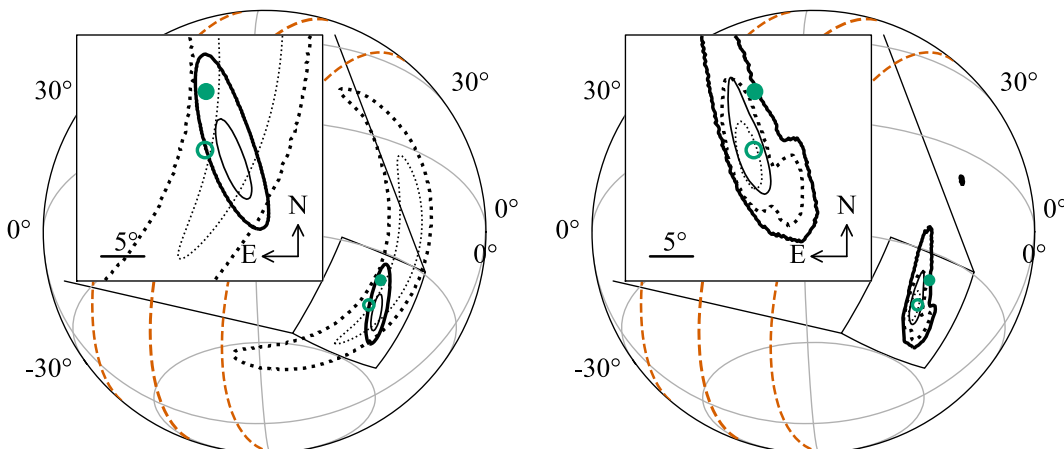


**Figure 1.** LEFT – Initial BAYESTAR sky map for GW170814 from GCN 21474, showing the LIGO only contours (dotted), joint LIGO–Virgo contours (solid), Abell 3084 (filled circle), and SMACS J0304.3 – 4401 (open). RIGHT – Initial LALINFERENCe sky map from GCN 21493 (solid) and most recent LALINFERENCe sky map from Abbott et al. (2018b; dotted), both based on LIGO–Virgo data, and the locations of both clusters. SMACS J0304.3 – 4401 (open circle) is closer to the peak of the sky localization than Abell 3084 (filled) in the revised maps. In both panels, the 90 (50) per cent credible region is shown as the thicker (thinner) contour, and galactic latitudes of  $\pm 20^\circ$  are indicated by the dashed lines.

**Table 2.** Follow-up observations of strong-lensing clusters within sky localization of GW170814.

Visit	Start of observation (UTC)	Airmass <sup>a</sup>	Integration time (ks)	Seeing <sup>b</sup> (arcsec)	Sensitivity <sup>c</sup>
GMOS OBSERVATIONS OF ABELL 3084					
1	2017 August 15, 06:40:40	1.29	2.9	0.72	24.7
2	2017 August 17, 07:50:52	1.09	2.3	0.49	25.2
3	2017 August 18, 06:14:13	1.33	3.1	0.81	24.8
4	2017 August 21, 07:09:38	1.05	3.1	0.76	24.9
5	2017 August 28, 07:44:48	1.03	3.1	0.84	24.9
GMOS OBSERVATIONS OF SMACS J0304.3 – 4401					
1	2017 August 18, 07:23:35	1.14	2.3	1.01	24.9
2	2017 August 21, 05:58:47	1.35	3.1	0.88	25.1
3	2017 August 27, 08:02:50	1.04	2.9	0.97	25.0
MUSE OBSERVATIONS OF ABELL 3084					
1	2017 August 17, 08:02:13	1.10	2.9	0.85	25.8
2	2017 August 19, 07:46:50	1.12	2.9	0.82	25.9

<sup>a</sup> The airmass at the mid-point of the observation.

<sup>b</sup> Mean full width at half-maximum of point sources in the reduced data, with a typical error on the mean of  $\sim 0.02$  arcsec.

<sup>c</sup>  $5\sigma$  point source sensitivity within a photometric aperture of diameter 2 arcsec, estimated from the magnitude at which the median photometric uncertainty is 0.2 magnitudes. The sensitivity of the MUSE observations is stated in the F606W-band.

occasions – August 18 and 21. The overall aim was to observe for  $\sim 45$  min on each night, with the exposure times and the number of exposures adjusted to suit the Moon phase and overhead conditions. The individual exposures were offset from each other randomly within a square region of full width 30 arcsec. Observations were performed in the *i*-band in order to minimize the impact of the Moon on the sensitivity of the observations, and to probe rest-frame V-band emission from putative lensed GWs at  $z \gtrsim 0.5$ .

We triggered a rapid ToO on VLT with MUSE within 3 h after LVC announced the detection of GW170814. This observation was executed at the telescope on 2017 August 17 UTC, and repeated on 2017 August 20 UTC. The delay between our trigger and the first MUSE observation was due to a combination of visitor mode time and engineering time on the intervening nights. Each observation comprised three exposures of duration 980 s and spanned the wavelength range  $475 \text{ nm} < \lambda < 930 \text{ nm}$ .

All of the GMOS and MUSE data were obtained at high elevation and with excellent seeing of  $0.5 \text{ arcsec} \leq \text{FWHM} \leq 1 \text{ arcsec}$ . Details of the GMOS and MUSE observations are listed in Table 2, and the reduction of GMOS and MUSE data is described in Sections 2.5 and 2.6, respectively.

## 2.5 GMOS data reduction

Individual GMOS exposures were de-biased, dark-subtracted, flat-fielded, and sky-subtracted in the standard manner using the GEMINI package in IRAF, to produce both a single science frame comprising the mosaiced individual chips, and a bad-pixel map, for each exposure. The bad-pixel maps were applied to the science frames and the individual masked science frames were then combined into a single stacked frame per visit using the IMCOMBINE task in IRAF. The full width at half-maximum of point sources in the reduced frames is consistently subarcsecond (Table 2). The reduced and stacked frames were aligned with the first visit for that target to a typical root-mean-square residual accuracy of 0.03 pixels using the IRAF tasks GEOMAP and GEOTRAN.

We searched the available USNO and GSC catalogues for sources of well calibrated *i*-band magnitude within the field of view of our

GMOS data. The size and depth of the GMOS imaging even in short exposures meant that there was no overlap between unsaturated bright stars as seen by Gemini and faint stars measured in all-sky surveys. We therefore calibrated the GMOS frames by measuring the  $(V_{606} - i)$  colours of sources detected in both the archival *HST*/ACS data and our GMOS data, and selecting the photometric zero-point that yields the correct colours for massive early-type galaxies in Abell 3084 and SMACS J0304.3 – 4401, respectively. These colours were computed using the EZGAL code,<sup>3</sup> using a single stellar population that formed at high redshift and evolved passively to the relevant cluster redshifts based on the Bruzual & Charlot (2003) population-synthesis code. The predicted colours are insensitive to the fine details of how we choose the formation redshift and the metallicity. We show an example  $(V_{606} - i)/i$  colour-magnitude diagram for one of the observations of Abell 3084 in Fig. 2.

## 2.6 MUSE data reduction

The MUSE observations were reduced using version 2.0 of the data reduction software (Weilbacher et al. 2014). The process includes basic calibration (bias removal, flat-fielding, wavelength, and geometrical calibration) and the production of datacubes for each exposure following sky subtraction, flux calibration, and telluric correction. These datacubes were matched in astrometry to the relevant *HST* observation discussed in Section 2.3. In all cases, only a constant offset in right ascension and declination was applied, as no significant rotation was found. The measured offsets and rotation were applied back to the original list of pixels (the pixel table), so that the datacubes can be produced in a single interpolation step to limit the effect on the noise properties. Each exposure’s datacube was treated for sky subtraction residuals using the PCA method implemented in the ZAP v2.0 software (Soto et al. 2016). We then combined all zapped exposures taken during each of the two observations.

<sup>3</sup>[www.baryons.org/ezgal/](http://www.baryons.org/ezgal/)

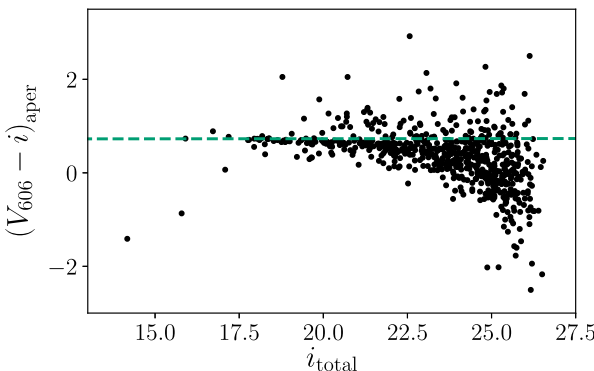


**Figure 2.** Example colour–magnitude diagram for Abell 3084 based on our GMOS and archival *HST*/ACS data. The horizontal dashed line shows the predicted colour of a single stellar population that formed at high redshift and evolved passively to the cluster redshift ( $z = 0.22$ ). The photometric zero-point of the GMOS frame was chosen to match the colour of the sequence of massive ( $i < 20$ ) cluster early-type galaxies to this prediction.

We assessed the image quality of the MUSE observations by performing a Moffat spatial fit of the bright unsaturated stars in each exposure. The seeing was stable in each night with average values provided in Table 2. We also estimated the cloud extinction to be just a few per cent and thus negligible, based on a comparison between MUSE pseudo-F606W frames (see Section 3.1) and relevant *HST* frames.

### 3 ANALYSIS AND RESULTS

#### 3.1 Difference images

We normalized each reduced and stacked GMOS frame to an exposure time of 1 s, and then matched the image quality between visits using the PSFMATCH task in IRAF. The point spread function (PSF) model was empirical and based on 10 isolated, unsaturated, high signal-to-noise ratio stars in the vicinity of the strong-lensing region of each frame. These matched frames were then subtracted from each other in pairs to produce difference images, examples of which are shown in Figs 3 and 4.

The wavelength range of the MUSE datacube ( $475 < \lambda < 930$  nm) obtained from our observations of Abell 3084 enables great freedom in the choice of reference image when constructing a difference image. We selected the *HST*/ACS observation through the F606W filter (Section 2.3) as the reference image. We therefore created a F606W pseudo-image from the MUSE datacube for each night upon which we observed Abell 3084, by multiplying the datacubes with the transmission curve of the F606W filter, and integrating under the transmission curve. The difference images were then produced by minimizing residuals in all detected sources, following a similar procedure described by Bacon et al. (2017) in the MUSE observations of the Ultra Deep Field. This optimization is performed over the Moffat model of the MUSE PSF, a possible astrometric shift between the two images, and the sky background level and average sky transmission. An example of difference image is shown in Fig. 3.

#### 3.2 Searching for transients in imaging data

We searched the difference images for transient sources both manually and automatically. The manual search was performed by

three authors (GPS, MB, AR), and identified no sources consistent with being a point source in the difference images. The only sources found were either residuals from the PSF matching close to the centres of bright galaxies, artefacts related to saturated stars, or a small number of residual bad pixels and cosmic rays. The automated search was performed with SExtractor (Bertin & Arnouts 1996), and found no sources other than PSF matching residuals and artefacts relating to saturated stars.

To calibrate the sensitivity of our GMOS search for candidate transients, we injected fake transients into the data in the following manner, and attempted to recover them both manually and automatically. We cut out  $31 \times 31$  pixel stamps from the GMOS data around the same, unsaturated, high signal-to-noise, stars used for the image quality matching. Each injected source was randomly chosen to be one of these bright star stamps, with the flux scaled accordingly, and shot noise added. To test the efficacy of manual recovery, we generated synthetic data sets, each containing (randomly and unknown to those searching) between 0 and 10 injected sources, with  $i$ -band magnitudes drawn uniformly from the range  $21 < i < 27$ . All injected sources with  $i < 25$  were identified by at least two searchers, while no sources with  $i > 25$  were identified by anyone. These results were independent of whether sources were injected randomly within 20 arcsec of the brightest cluster galaxy (BCG), or into faint background galaxies (including the spectroscopically confirmed multiply imaged galaxies) following the methods described by Sharon et al. (2010). We show examples of fake  $i = 25$  point sources injected in to our data in Fig. 5.

To test the automated search, we generated  $10^4$  synthetic datasets comprising sources injected at each integer magnitude in the range  $21 \leq i \leq 26$ . SExtractor was then run on these synthetic datasets, with the source being detected if SExtractor finds a source within 0.5 arcsec of the injected source location. At small angular separations from the BCG ( $\theta_{\text{BCG}}$ ), the probability of sources being detected is low due to the residuals in the difference images (Fig. 6). The source recovery rate at the very centre (within  $< 0.5$  arcsec of the BCG) is artificially boosted because SExtractor detects the residuals at the centre of the BCG (in the absence of an injected source) as a source. However, these scales are generally smaller than the high-magnification region close to the radial critical curve, and therefore the residuals at the centre of the BCG are not a major limiting factor in our analysis.

Sources at the typical  $5\sigma$  point source sensitivity of our GMOS data ( $i \simeq 25$ ) are detected with the expected  $\sim 80$  per cent completeness at  $\theta_{\text{BCG}} \gtrsim 5$  arcsec, and sources at  $i \simeq 24$  are detectable right down to angular separations of a few arcseconds. We put this into context by plotting in grey in Fig. 6 the solid angle that is magnified by the amount required to reinterpret the strain signal from GW170814 as coming from  $z = 0.764$ , which is the redshift at which the lens model of Abell 3084 is most robust (Section 2.3), also taking into account the uncertainty on the luminosity distance to GW170814. Use of  $z = 0.764$  is by way of example only, and motivated by not wishing to extrapolate the lens model to redshifts at which it is not constrained. The peaks at  $\theta_{\text{BCG}} \simeq 4$  arcsec and  $\theta_{\text{BCG}} \simeq 12$  arcsec correspond to the radial and tangential critical curves, respectively (see the inner and outer red curves in Fig. 3). Our search is therefore sensitive at  $>80$  per cent completeness to point sources at  $i \lesssim 24$  that are adjacent to either critical curve and to point sources at  $i \lesssim 25$  that are adjacent to the tangential critical curve.

We performed similar manual and automated tests with MUSE images, injecting sources into the inner 15 arcsec of the Abell

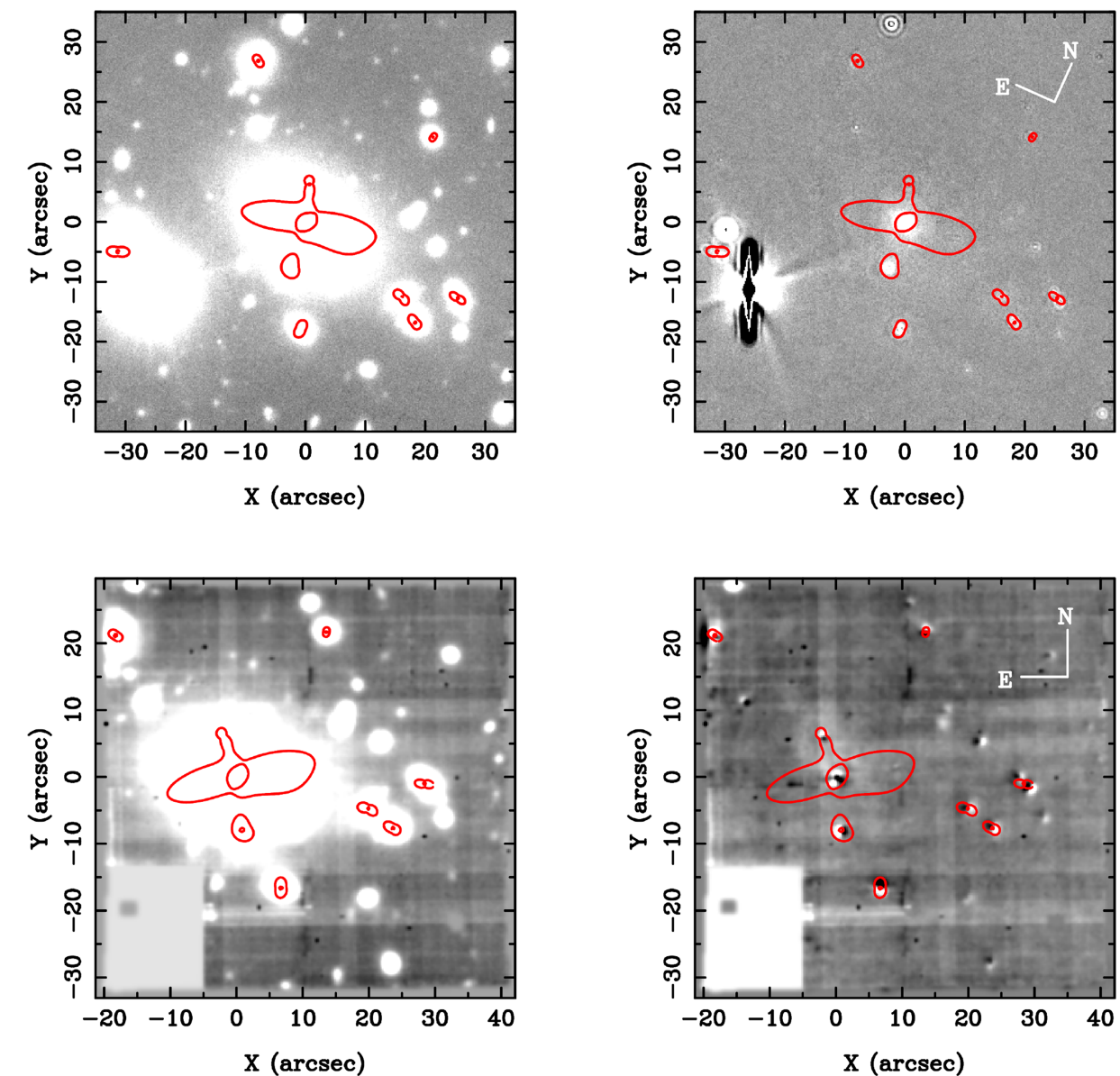


**Figure 3.** Central region of Abell 3084, with the BCG at the origin in each panel. Examples from our data shown as follows: GMOS *i*-band observation (top left); GMOS-based difference image (top right); MUSE observation convolved with the F606W filter (bottom left); MUSE/*HST*-based difference image (bottom right). The red curves show the critical curves for  $z_S = 0.764$ .

3084 MUSE/*HST* difference image, obtaining similar results to the GMOS tests described above. As a consequence of the smaller field of view of MUSE compared to GMOS, we did not have a large number of bright stars to use as templates for point sources, but instead used the best-fitting Moffat profile discussed in Section 2.6. We interpret the slight shortfall in the fraction of fake sources that are recovered from the MUSE/*HST* difference images relative to the GMOS images as being caused by the flux sensitivity of the short *HST* observation being inferior to that of the MUSE observations, after smoothing the *HST* data to match the ground-based seeing.

### 3.3 Searching for transients in MUSE data cubes

In addition to the search for continuum sources based on pseudo-images created from the MUSE datacubes, we have performed an

automatic search for emission lines across all wavelengths. This is done using the MUSELET detection software, which has been used in the past to automatically search for line emitters in MUSE blank fields (Drake et al. 2017a,b) as well as lensing cluster fields (Lagattuta et al. 2017; Mahler et al. 2018). MUSELET is publicly available as part of the MUSE Python Data Analysis Framework (Conseil et al. 2016) software suite. It is a SExtractor-based detection tool based on a continuum-subtracted datacube where each wavelength plane is replaced by its corresponding narrow-band image, optimized for the detection of typical  $\text{FWHM} = 150 \text{ km s}^{-1}$  line width line sources. The sensitivity of MUSELET in recovering point-source line emitters has been extensively tested by Drake et al. (2017b) in the MUSE Ultra Deep Field (Bacon et al. 2017), and we rescale their results to the exposure times of individual datacubes in each night. The values show that our search

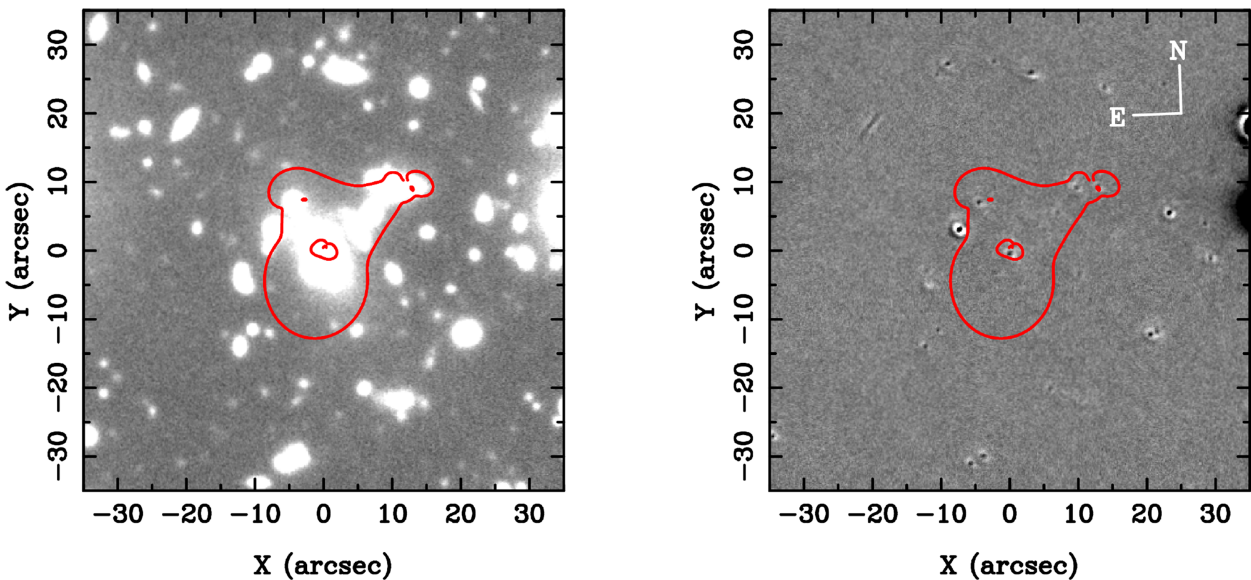


**Figure 4.** Central region of SMACS J0304.3 – 4401, centred on the BCG. Examples from our data are shown as follows: GMOS  $i$ -band observation (left); GMOS-based difference image (right). The red curve is the tangential critical curve for  $z_S = 1.963$ .

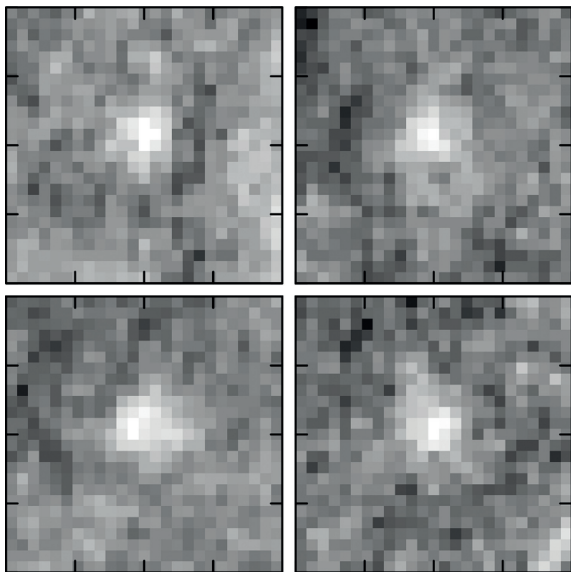


**Figure 5.** Example fake  $i = 25$  point sources that were injected into the GMOS observations of Abell 3084. Each panel is  $4 \times 4$  arcsec.

is complete for line fluxes brighter than  $5 \times 10^{-17}$  erg s $^{-1}$  cm $^{-2}$  (Fig. 7).

Removing obvious false detections (sharper than the spatial and/or spectral PSF) through visual inspection, we compare the detection of line emitters found in each datacube as well as the combination of both nights with the reference *HST* image. The only sources appearing as line emitters in MUSE and absent from *HST* are clear Lyman- $\alpha$  emitters with strong equivalent width identified from the shape of their spectral lines and/or as multiple images.

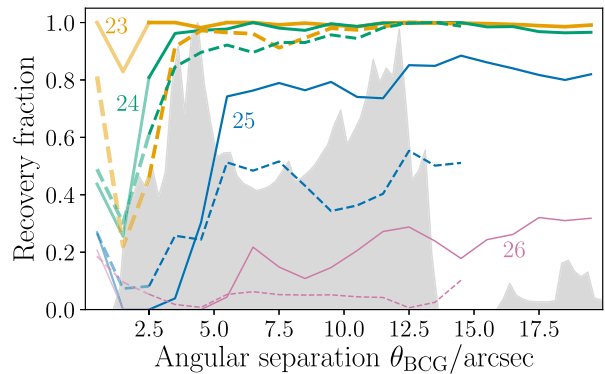


**Figure 6.** The recovery fraction of injected sources with different  $i$ -band magnitudes (as labelled), as a function of angular separation from the BCG. The solid lines show fractions for sources injected into GMOS observations of Abell 3084, while the dashed lines are for sources injected into the MUSE/*HST* data for the same cluster. The lines are faded at small radii where the recovery of injected sources is confused by the presence of structured residuals near the BCG centre. The radial distribution of image-plane solid angle magnified sufficiently to reinterpret the LIGO–Virgo detection of GW170814 as originating from  $z = 0.764$  is shown by the grey area.

## 4 DISCUSSION

We now discuss the empirical sensitivity of our observations of strong-lensing cluster cores in the context of the plausible EM counterparts to CBC GW sources. We first discuss the cancellation of the inverse square law by lens magnification for strongly lensed point source EM counterparts to GWs (Section 4.1), and then apply this to kilonova-like EM counterparts (Section 4.2), and EM counterparts that might resemble emission from known low mass X-ray binaries within the Milky Way during outburst (Section 4.3).

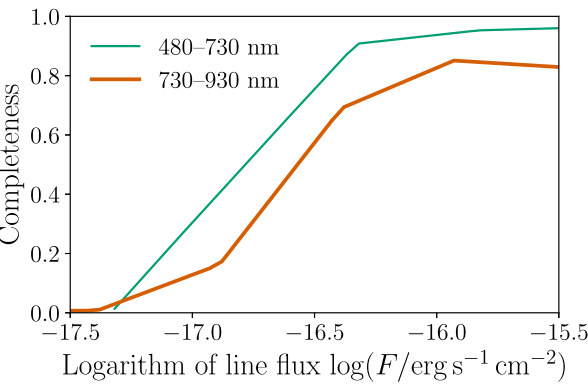


**Figure 7.** Emission line sensitivity in our search for transients in the individual (per night) MUSE datacubes. Presented is the average completeness level of recovering emission line point sources with MUSELET as a function of line flux, which slightly varies across the cube as a function of the wavelength range.

#### 4.1 The inverse square law and lens magnification

Consider a hypothetical GW source that is inferred to be at a luminosity distance  $D_{L,\mu=1}$  assuming  $\mu = 1$ , and that has an EM counterpart of absolute magnitude  $M$  in an arbitrary pass band. If this is actually a distant source at  $D_{L,\text{true}}$  that is gravitationally magnified by  $\mu > 1$ , then its apparent magnitude in a pass band that probes the same rest-frame wavelength range as the pass band relevant to  $M$  (or, equivalently, assuming  $k$ -corrections are negligible), is given by

$$m = M + 5 \log(D_{L,\text{true}}) - 5 - 2.5 \log(\mu), \quad (1)$$

with  $D_{L,\text{true}}$  expressed in units of parsecs. As discussed in Section 1, the lens magnification that appears in equation (1) is given by

$$\mu = \left( \frac{D_{L,\text{true}}}{D_{L,\mu=1}} \right)^2. \quad (2)$$

The apparent magnitude of the EM counterpart of a lensed GW therefore depends only on the absolute magnitude of the counterpart and the luminosity distance at which the source is placed when (incorrectly) assuming  $\mu = 1$ :

$$m = M + 5 \log(D_{L,\mu=1}) - 5. \quad (3)$$

The apparent magnitude of a lensed EM counterpart is therefore set by the initial analysis of the signal detected by LIGO–Virgo assuming  $\mu = 1$ . Therefore, observations capable of detecting a given EM counterpart located at  $D_{L,\mu=1}$  are also able to detect the same type of counterpart if it is lensed, independent of the true redshift.

#### 4.2 Kilonovae

Optical follow-up observations of BH–BH sources have so far generally aimed to achieve the sensitivity required to detect a kilonova at  $D_{L,\mu=1}$  (e.g. Cowperthwaite et al. 2016; Soares-Santos et al. 2016; Arcavi et al. 2017; Yoshida et al. 2017; Doctor et al. 2018; Utsumi et al. 2018). We therefore consider how bright a kilonova-like counterpart to GW170814 would have been if it had been lensed. The kilonova counterpart to GW170817 had an absolute magnitude in optical bands of  $M \lesssim -13.5$  in the few days after discovery (e.g. Villar et al. 2017; Arcavi 2018). We therefore adopt  $M \simeq -13.5$  in the rest-frame  $B/V/R$ -bands as a template

for our calculations. If GW170814 was strongly lensed, and had a kilonova-like EM counterpart, then based on its inferred luminosity distance,  $D_{L,\mu=1} = 580^{+160}_{-210}$  Mpc (Section 2.2), it would have an apparent magnitude of  $m \simeq 24\text{--}26$  in the rest-frame  $B/V/R$ -bands independent of its luminosity distance. Our observations reach a depth of  $m \simeq 25\text{--}26$  (Table 2), with a sensitivity to transient sources in our difference image analysis of  $m \simeq 24\text{--}25$  at  $\gtrsim 80$  per cent completeness. These sensitivities are in the observer-frame  $V_{606}$  – and  $i$  bands, and can thus be compared with the rest-frame bands quoted above for sources at  $z \simeq 1$ . It should therefore have been possible to detect a kilonova-like EM counterpart if GW170814 was strongly lensed by one of the clusters that we observed.

A kilonova-like EM counterpart to GW170814 is more plausible if GW170814 actually comprised one or more NS in an NS–NS or NS–BH system. The primary means of identifying a GW source as an NS–NS, NS–BH, or BH–BH is from the inferred component masses, as NSs have a maximum mass of  $< 3 M_\odot$  (Rhoades & Ruffini 1974; Kalogera & Baym 1996; Margalit & Metzger 2017).<sup>4</sup> For a particular GW signal, the inferred rest-frame mass of the compact objects is inversely proportional to  $(1+z)$ , where  $z$  is the redshift of the GW source. Therefore, the rest-frame mass of GW sources would be revised downwards from the initial estimate by LIGO–Virgo, if they are subsequently identified as being strongly lensed. The source frame masses of the individual BHs that comprise GW170814 are  $30.7^{+5.7}_{-3.0} M_\odot$  and  $25.3^{+2.9}_{-4.1} M_\odot$  (Abbott et al. 2018b), which correspond to  $\sim 34$  and  $\sim 28 M_\odot$  in the detector frame, i.e.  $\gtrsim 9$  times larger than the maximum NS mass. Therefore, if GW170814 were strongly lensed, then it would have to be at  $z \gtrsim 8$  for one or both of the two BHs to be reinterpreted as an NS. This implies a lens magnification of  $\mu \gtrsim 10^4$ , which is possible for point sources located behind galaxy cluster lenses (Miralda-Escude 1991; Diego et al. 2018; Kelly et al. 2018; Rodney et al. 2018). Our observations and difference image analysis yielded no transient sources in the strong-lensing regions of Abell 3084 and SMACS J0304.3 – 4401 down to  $m = 25$ . Therefore, if we assume that the rest-frame ultraviolet luminosity of a kilonova-like EM counterpart is similar to the rest-frame optical luminosity of GW170817, we can exclude the interpretation of GW170817 as an NS–NS or NS–BH merger at  $z > 8$  that has been strongly lensed by either of these clusters.

More generally, our analysis shows that the cancellation of the inverse square law by the degeneracy between luminosity distance and lens magnification has important implications for the EM follow-up of GW sources. Specifically, that the detection of EM counterparts to lensed NS–NS and NS–BH sources is within the reach of deep ground-based optical observations with 8-m class telescopes. Our difference image analysis is sensitive to transients as faint as  $i \simeq 25$  and are thus sensitive to kilonova-like counterparts to lensed sources that are initially identified at  $D_{L,\mu=1} \simeq 500$  Mpc, independent of their true distance.

In the future, it may be more fruitful to search for lensed optical kilonova-like counterparts to GW sources initially identified as low-mass BH–BH systems, with individual BH masses of  $< 10 M_\odot$  because such lower masses imply a less extreme lens magnification. For example, GW170608 (Abbott et al. 2017h) would have been an

<sup>4</sup>NSs could also be disambiguated from the imprint of tidal effects on the signal. These are difficult to measure, and could not be conclusively identified for GW170817 despite its high signal-to-noise ratio, without assuming that the source comprised NSs (Abbott et al. 2017c, 2018c).

ideal target for our observing programme, if we had commenced our observing programmes at VLT and Gemini just a few months earlier. GW170608 comprised (assuming  $\mu = 1$ ) two BHs of masses  $10.9_{-1.7}^{+5.3} M_\odot$  and  $7.6_{-2.1}^{+1.3} M_\odot$ , respectively, at  $z = 0.07_{-0.02}^{+0.02}$ , which corresponds to  $D_{L,\mu=1} = 320_{-110}^{+120}$  Mpc (Abbott et al. 2018b). Following the reasoning outlined above, it is possible that this is a lensed NS–NS source at  $z \simeq 2\text{--}5$ , which is magnified by  $\mu \simeq 10^3\text{--}10^4$ . This level of magnification is similar to that suffered by the strongly lensed individual blue giant star dubbed ‘Icarus’ (Kelly et al. 2018). A kilonova-like counterpart to GW170608 would have an apparent magnitude of  $m \simeq 24$  if it is strongly lensed, independent of its redshift. This is brighter than discussed above for GW170814, but still sufficiently faint to be beyond the reach of most of the current generation of wide-field searches for EM counterparts (Section 2.1).

### 4.3 Low mass X-ray binaries

We also consider the possibility of detecting an EM counterpart that is much fainter than a kilonova. A BH–BH merger in vacuum is not expected to emit any EM radiation; however, numerous theoretical ideas for EM counterparts to BH–BH mergers not in vacuum have been proposed following the detection of GW150914 (e.g. Li et al. 2016; Loeb 2016; Lyutikov 2016; Morsony, Workman & Ryan 2016; Murase et al. 2016; Perna, Lazzati & Giacomazzo 2016; Woosley 2016; Yamazaki, Asano & Ohira 2016; Bartos et al. 2017; Dai, McKinney & Miller 2017; de Mink & King 2017; Janiuk et al. 2017; Ryan & MacFadyen 2017; Stone, Metzger & Haiman 2017). By way of illustration, we adopt a simple model of an EM counterpart, apply equation (3), and compare with the sensitivity of our search.

We speculate that low mass BH X-ray Binaries (LMXRB) during outburst in the Milky Way could provide an illustrative upper limit on the brightness of the EM counterparts to BH–BH mergers. The brightest LMXRB seen to date is V404 Cyg, with a BH mass of  $9 M_\odot$  and peak extinction corrected absolute  $V$ -band magnitude during outburst of  $M_V \simeq -4.7$  (e.g. van Paradijs & McClintock 1994; Bernardini et al. 2016). We further assume that the luminosity of the accretion disc is proportional to the mass of the BH, and the accretion rate as a fraction of the Eddington limit. Therefore, combining these assumptions with the dependence of BH mass on redshift (discussed in Section 1), gives the following expression for the estimated absolute magnitude  $M$  of the EM counterpart to a lensed BH–BH merger:

$$M = M_0 - 2.5 \log \left( \frac{\Lambda}{\Lambda_0} \cdot \frac{M_{f,\mu=1}}{M_0} \cdot \frac{1 + z_{\mu=1}}{1 + z} \right), \quad (4)$$

where  $z$  is the true redshift of the lensed BH–BH,  $M_{f,\mu=1}$  is the final BH mass of a BH–BH merger inferred assuming  $\mu = 1$ ,  $\Lambda$  denotes accretion rate as a fraction of the Eddington limit, and we adopt  $M_0 = -4.7$ ,  $M_0 = 9 M_\odot$ , and  $\Lambda_0 = 1$  for V404 Cyg. Substituting equation (4) into equation (3), and adopting  $M_{f,\mu=1} \simeq 53 M_\odot$ ,  $z_{\mu=1} \simeq 0.12$  for GW170814 (Abbott et al. 2018b), a nominal source redshift of  $z \simeq 1$ , and  $\Lambda = 1$ , gives  $m \simeq 33$ . This is a factor  $\simeq 10^3\text{--}10^4$  fainter than the transient point sources that we are able to recover in our difference imaging (Section 3), which is unsurprising given that we did not set out to detect such faint EM counterparts. Moreover, to underline how challenging any possible detection of an EM counterpart to a BH–BH would be,  $\Lambda \gtrsim 10$  would be required to bring the apparent magnitude of a source within reach of an observation of depth comparable with

the Hubble Ultra Deep Field, i.e.  $m \simeq 30$ . Alternatively, follow-up observations of a GW170814-like source initially placed at  $D_{L,\mu=1} = 170$  Mpc and with  $\Lambda = 1$  would also be detectable at  $m \simeq 30$ , based on this speculative V404 Cyg-like scenario. Finally, in all of this discussion, we have assumed that  $k$ -corrections are negligible, as the absolute magnitudes are in the (effectively) rest-frame  $V$ -band of sources at  $z \simeq 1$  that we observe in the  $i$ -band.

## 5 SUMMARY

In the nights immediately following the announcement of the detection of GW170814, we observed two strong-lensing cluster cores – Abell 3084 and SMACS J0304.3 – 4401 – identified using the sky localization available from the LVC. Our observations were conducted with the GMOS and MUSE instruments on the Gemini-South telescope and VLT, respectively. The data reach a sensitivity to point sources of  $m(5\sigma) \simeq 25\text{--}26$ , and our search for transient sources is sensitive down to  $m = 25$  in the continuum and line fluxes of  $5 \times 10^{-17} \text{ erg s}^{-1} \text{ cm}^{-2}$ . We detect no credible candidate transient sources in the data down to these limits. This is the most sensitive search to date for EM counterparts to GW sources, independent of considerations of possible lens amplification.

The lens magnification suffered by a lensed GW source cancels out the inverse square law, and therefore the apparent magnitude of a point source EM counterpart of given luminosity is set by the luminosity distance inferred from the GW data assuming no lens magnification. The apparent magnitude of EM counterparts to lensed GW sources is independent of the true redshift of the source. We therefore show, as a proof of concept, that we can exclude the idea that GW170814 is an NS–BH or NS–NS source at  $z > 8$  that is lensed by either of these clusters. We also show that observations with 30-m class and/or space-based telescopes will be required to conduct meaningful searches for lensed EM counterparts to BH–BH sources. We will consider the details of such observing strategies, and those required for lensed NS–NS and NS–BH sources in a future article.

In summary, we have confirmed the feasibility of searching for EM counterparts to candidate lensed GW sources with ground-based 8-m class telescopes, and described some important considerations for future development of this new observing strategy within the rapidly growing field of GW astronomy.

## ACKNOWLEDGEMENTS

GPS dedicates this article to the memory of Robert Smith, and thanks Olivia Mueller for her support during August 2017. GPS also thanks Gary Mamon and colleagues at the Institut d’Astrophysique de Paris for their warm welcome during the later stages of writing this article, and Alberto Vecchio for his advice and support. We thank Iair Arcavi and Leo Singer for assistance with Fig. 1, Alyssa Drake for providing us with the results of completeness tests to blindly detect line emitters within MUSE datacubes using MUSELET, and Chris Done and Sylvain Chaty for helpful discussions about low mass X-ray binaries. We thank the staff and Directors of the Gemini and La Silla Paranal Observatories for their superb support of our observing programmes and awards of Director’s Discretionary time, respectively. We acknowledge support from the Science and Technology Facilities Council through the following grants: ST/N000633/1 (GPS, MB, CPLB, WMF), ST/L00075X/1, ST/P000451/1 (MJ), and ST/K005014/1 (JV). JR acknowledges

support from the ERC starting grant 336736-CALENDS. RM acknowledges support from the Royal Society.

## REFERENCES

- Abbott B. P. et al., 2016a, *Phys. Rev. X*, 6, 041015  
 Abbott B. P. et al., 2016b, *Living Rev. Relativ.*, 19, 1  
 Abbott B. P. et al., 2016c, *Phys. Rev. Lett.*, 116, 061102  
 Abbott B. P. et al., 2016d, *Phys. Rev. Lett.*, 116, 221101  
 Abbott B. P. et al., 2016e, *Phys. Rev. Lett.*, 116, 241102  
 Abbott B. P. et al., 2016f, *ApJ*, 818, L22  
 Abbott B. P. et al., 2016g, *ApJ*, 826, L13  
 Abbott B. P. et al., 2017a, *Phys. Rev. Lett.*, 118, 221101  
 Abbott B. P. et al., 2017b, *Phys. Rev. Lett.*, 119, 141101  
 Abbott B. P. et al., 2017c, *Phys. Rev. Lett.*, 119, 161101  
 Abbott B. P. et al., 2017d, *Nature*, 551, 85  
 Abbott B. P. et al., 2017e, *ApJ*, 848, L12  
 Abbott B. P. et al., 2017f, *ApJ*, 848, L13  
 Abbott B. P. et al., 2017g, *ApJ*, 850, L40  
 Abbott B. P. et al., 2017h, *ApJ*, 851, L35  
 Abbott B. P. et al., 2018a, preprint ([arXiv:1811.12940](https://arxiv.org/abs/1811.12940))  
 Abbott B. P. et al., 2018b, preprint ([arXiv:1811.12907](https://arxiv.org/abs/1811.12907))  
 Abbott B. P. et al., 2018c, *Phys. Rev. X*, 9, 011001–1  
 Ade P. A. R. et al., 2016, *A&A*, 594, A13  
 Agnello A., Grillo C., Jones T., Treu T., Bonamigo M., Suyu S. H., 2018, *MNRAS*, 474, 3391  
 Arcavi I., 2018, *ApJ*, 855, L23  
 Arcavi I. et al., 2017, *ApJ*, 848, L33  
 Bacon R. et al., 2017, *A&A*, 608, A1  
 Bartos I., Kocsis B., Haiman Z., Márka S., 2017, *ApJ*, 835, 165  
 Bauswein A., Just O., Janka H.-T., Stergioulas N., 2017, *ApJ*, 850, L34  
 Bernardini F., Russell D. M., Koljonen K. I. I., Stella L., Hynes R. I., Corbel S., 2016, *ApJ*, 826, 149  
 Berry C. P. L. et al., 2015, *ApJ*, 804, 114  
 Bertin E., Arnouts S., 1996, *A&AS*, 117, 393  
 Böhringer H. et al., 2004, *A&A*, 425, 367  
 Bruzual G., Charlot S., 2003, *MNRAS*, 344, 1000  
 Chatzioannou K., Yunes N., Cornish N., 2012, *Phys. Rev. D*, 86, 022004  
 Chen G. C.-F. et al., 2018, *MNRAS*, 481, 1115  
 Christensen L. et al., 2012, *MNRAS*, 427, 1973  
 Collett T. E., Bacon D., 2017, *Phys. Rev. Lett.*, 118, 091101  
 Conseil S., Bacon R., Piquerias L., Shepherd M., 2016, preprint ([arXiv: 1612.05308](https://arxiv.org/abs/1612.05308))  
 Coughlin M. W. et al., 2018, *MNRAS*, 478, 692  
 Coulter D. A. et al., 2017, *Science*, 358, 1556  
 Cowperthwaite P. S. et al., 2016, *ApJ*, 826, L29  
 Dai L., McKinney J. C., Miller M. C., 2017, *MNRAS*, 470, L92  
 de Mink S. E., King A., 2017, *ApJ*, 839, L7  
 Del Pozzo W., Berry C. P. L., Ghosh A., Haines T. S. F., Singer L. P., Vecchio A., 2018, *MNRAS*, 479, 601  
 Diego J. M. et al., 2018, *ApJ*, 857, 25  
 Doctor Z. et al., 2019, *ApJ*, 873, 24  
 Drake A. B. et al., 2017a, *MNRAS*, 471, 267  
 Drake A. B. et al., 2017b, *A&A*, 608, A6  
 Fan X., Messenger C., Heng I. S., 2014, *ApJ*, 795, 43  
 Fan X.-L., Liao K., Biesiada M., Piórkowska-Kurpas A., Zhu Z.-H., 2017, *Phys. Rev. Lett.*, 118, 091102  
 Fohlmeister J. et al., 2007, *ApJ*, 662, 62  
 Gehrels N., Cannizzo J. K., Kanner J., Kasliwal M. M., Nissanke S., Singer L. P., 2016, *ApJ*, 820, 136  
 Hanna C., Mandel I., Vossen W., 2014, *ApJ*, 784, 8  
 Hannuksela O. A., Haris K., Ng K. K. Y., Kumar S., Mehta A. K., Keitel D., Li T. G. F., Ajith P., 2019, preprint ([arXiv:1901.02674](https://arxiv.org/abs/1901.02674))  
 Hilbert S., White S. D. M., Hartlap J., Schneider P., 2008, *MNRAS*, 386, 1845  
 Inada N. et al., 2003, *Nature*, 426, 810  
 Inada N. et al., 2005, *AJ*, 130, 1967  
 Inada N. et al., 2006, *AJ*, 131, 1934  
 Inada N. et al., 2007, *AJ*, 133, 206  
 Inada N. et al., 2008, *AJ*, 135, 496  
 Inada N. et al., 2009, *AJ*, 137, 4118  
 Inada N., Oguri M., Rusu C. E., Kayo I., Morokuma T., 2014, *AJ*, 147, 153  
 Janiuk A., Bejger M., Charzyński S., Sukova P., 2017, *New Astron.*, 51, 7  
 Kalogera V., Baym G., 1996, *ApJ*, 470, L61  
 Kayo I. et al., 2007, *AJ*, 134, 1515  
 Kayo I., Inada N., Oguri M., Morokuma T., Hall P. B., Kochanek C. S., Schneider D. P., 2010, *AJ*, 139, 1614  
 Kelly P. L. et al., 2018, *Nat. Astron.*, 2, 334  
 Krolak A., Schutz B. F., 1987, *Gen. Relativ. Gravit.*, 19, 1163  
 Lagattuta D. J. et al., 2017, *MNRAS*, 469, 3946  
 Levan A. J. et al., 2017, *ApJ*, 848, L28  
 Li X., Zhang F.-W., Yuan Q., Jin Z.-P., Fan Y.-Z., Liu S.-M., Wei D.-M., 2016, *ApJ*, 827, L16  
 Liao K., Fan X.-L., Ding X., Biesiada M., Zhu Z.-H., 2017, *Nat. Commun.*, 8, 1148  
 LIGO Scientific Collaboration, Virgo Collaboration, 2017a, GRB Coordinates Network, Circular Service, No. 21474, (2017), 21474.  
 LIGO Scientific Collaboration, Virgo Collaboration, 2017b, GRB Coordinates Network, Circular Service, No. 21474, (2017), 21493.  
 Li S.-S., Mao S., Zhao Y., Lu Y., 2018, *MNRAS*, 476, 2220  
 Loeb A., 2016, *ApJ*, 819, L21  
 Lyutikov M., 2016, preprint ([arXiv:1602.07352](https://arxiv.org/abs/1602.07352))  
 Mahler G. et al., 2018, *MNRAS*, 473, 663  
 Margalit B., Metzger B. D., 2017, *ApJ*, 850, L19  
 McGreer I. D. et al., 2010, *AJ*, 140, 370  
 Miralda-Escude J., 1991, *ApJ*, 379, 94  
 More A. et al., 2016, *MNRAS*, 456, 1595  
 Morokuma T. et al., 2007, *AJ*, 133, 214  
 Morsony B. J., Workman J. C., Ryan D. M., 2016, *ApJ*, 825, L24  
 Murase K., Kashiyama K., Mészáros P., Shoemaker I., Senno N., 2016, *ApJ*, 822, L9  
 Ng K. K. Y., Wong K. W. K., Broadhurst T., Li T. G. F., 2018, *Phys. Rev. D*, 97, 023012  
 Nissanka S., Kasliwal M., Georgieva A., 2013, *ApJ*, 767, 124  
 Ofek E. O., Oguri M., Jackson N., Inada N., Kayo I., 2007, *MNRAS*, 382, 412  
 Oguri M. et al., 2004, *PASJ*, 56, 399  
 Oguri M. et al., 2005, *ApJ*, 622, 106  
 Oguri M. et al., 2008, *AJ*, 135, 520  
 Oguri M., 2010, *PASJ*, 62, 1017  
 Oguri M. et al., 2013, *MNRAS*, 429, 482  
 Pankow C., Chase E. A., Coughlin S., Zevin M., Kalogera V., 2018, *ApJ*, 854, L25  
 Perna R., Lazzati D., Giacomazzo B., 2016, *ApJ*, 821, L18  
 Repp A., Ebeling H., 2018, *MNRAS*, 479, 844  
 Rhoades C. E., Ruffini R., 1974, *Phys. Rev. Lett.*, 32, 324  
 Rodney S. A. et al., 2016, *ApJ*, 820, 50  
 Rodney S. A. et al., 2018, *Nat. Astron.*, 2, 324  
 Rusu C. E. et al., 2011, *ApJ*, 738, 30  
 Rusu C. E., Oguri M., Iye M., Inada N., Kayo I., Shin M.-S., Sluse D., Strauss M. A., 2013, *ApJ*, 765, 139  
 Ryan G., MacFadyen A., 2017, *ApJ*, 835, 199  
 Sharon K. et al., 2005, *ApJ*, 629, L73  
 Sharon K. et al., 2010, *ApJ*, 718, 876  
 Sharon K. et al., 2017, *ApJ*, 835, 5  
 Singer L. P. et al., 2014, *ApJ*, 795, 105  
 Singer L. P. et al., 2016, *ApJ*, 829, L15  
 Singer L. P. et al., 2016, *Phys. Rev. D*, 93, 024013  
 Smith G. P. et al., 2018a, Proceedings of the International Astronomical Union, IAU Symposium, Vol. 338, 98  
 Smith G. P., Jauzac M., Veitch J., Farr W. M., Massey R., Richard J., 2018b, *MNRAS*, 475, 3823  
 Soares-Santos M. et al., 2016, *ApJ*, 823, L33

- Soto K. T., Lilly S. J., Bacon R., Richard J., Conseil S., 2016, *MNRAS*, 458, 3210  
 Stone N. C., Metzger B. D., Haiman Z., 2017, *MNRAS*, 464, 946  
 Suyu S. H., Chang T.-C., Courbin F., Okumura T., 2018, *Space Sci. Rev.*, 214, 91  
 Tie S. S., Kochanek C. S., 2018, *MNRAS*, 473, 80  
 Utsumi Y. et al., 2018, *PASJ*, 70, 1  
 van Paradijs J., McClintock J. E., 1994, *A&A*, 290, 133  
 Veitch J. et al., 2012, *Phys. Rev. D*, 85, 104045  
 Veitch J. et al., 2015, *Phys. Rev. D*, 91, 042003  
 Villar V. A. et al., 2017, *ApJ*, 851, L21  
 Wang Y., Stebbins A., Turner E. L., 1996, *Phys. Rev. Lett.*, 77, 2875  
 Weilbacher P. M., Streicher O., Urrutia T., Pécontal-Rousset A., Jarno A., Bacon R., 2014, in Manset N., Forshay P., eds, ASP Conf. Ser. Vol. 485, Astronomical Data Analysis Software and Systems XXIII. Astron. Soc. Pac., San Francisco, p. 451  
 Woosley S. E., 2016, *ApJ*, 824, L10  
 Yamazaki R., Asano K., Ohira Y., 2016, *Prog. Theor. Exp. Phys.*, 2016, 051E01  
 Yoshida M. et al., 2017, *PASJ*, 69, 9

This paper has been typeset from a *TeX/LaTeX* file prepared by the author.